Publication Year	2022
Acceptance in OA	2025-05-16T14:32:19Z
Title	The Origin of the Unfocused XMM-Newton Background, Its Variability, and Lessons Learned for ATHENA
Authors	GASTALDELLO, Fabio, MARELLI, Martino, MOLENDI, SILVANO, BARTALUCCI, Iacopo, Patrick Kühl, Catherine E. Grant, GHIZZARDI, SIMONA, ROSSETTI, Mariachiara, DE LUCA, Andrea, TIENGO, ANDREA
Publisher's version (DOI)	10.3847/1538-4357/ac5403
Handle	http://hdl.handle.net/20.500.12386/37146
Journal	THE ASTROPHYSICAL JOURNAL
Volume	928

The Astrophysical Journal, 928:168 (11pp), 2022 April 1 https://doi.org/10.3847/1538-4357/ac5403

The Origin of the Unfocused XMM-Newton Background, Its Variability, and Lessons Learned for ATHENA

Fabio Gastaldello[1], Martino Marelli[1], Silvano Molendi[1], Iacopo Bartalucci[1], Patrick Kühl[2], Catherine E. Grant[3], Simona Ghizzardi[1], Mariachiara Rossetti[1], Andrea De Luca[1,4], and Andrea Tiengo[1,4,5]
[1] INAF/IASF-Milano, Via A. Corti 12, I-20133 Milano, Italy; fabio.gastaldello@inaf.it
[2] Christian-Albrechts-Universität zu Kiel, Leibnizstr. 11, D-24118 Kiel, Germany
[3] Kavli Institute for Astrophysics and Space Research, Massachusetts Institute of Technology, Cambridge, MA, USA
[4] INFN, Sezione di Pavia, Via A. Bassi 6, I-2700 Pavia, Italy
[5] Scuola Universitaria Superiore IUSS Pavia, piazza della Vittoria 15, I-27100 Pavia, Italy

Received 2021 November 22; revised 2022 February 8; accepted 2022 February 9; published 2022 April 6

Abstract

We analyzed the unexposed to the sky (outFOV) region of the MOS2 detector on board XMM-Newton covering 15 yr of data amounting to 255 Ms. We show convincing evidence that the origin of the unfocused background in XMM-Newton is due to energetic protons, electrons, and hard X-ray photons. Galactic cosmic rays are the main contributors as shown by the tight correlation (2.6% of total scatter) with the 1 GeV proton data of the SOHO EPHIN detector. Tight correlations are found with a proxy of the Chandra background rate, revealing the common source of background for detectors in similar orbits, and with the data of the EPIC Radiation Monitor, only when excluding Solar energetic particle events. The entrance to the outer electron belts is associated with a sudden increase in the outFOV MOS2 rate and a spectral change. These facts support the fact that MeV electrons can generate an unfocused background signal. The correlation between MOS2 outFOV data and the SOHO EPHIN data reveals a term constant in time and isotropic, similar to the one found in the study of the pn data. The most plausible origin of this component is hard unfocused X-ray photons of the cosmic X-ray background Compton scattering in the detector as supported by the strength of the signal in the two detectors with different thicknesses. Based on this physical understanding, a particle radiation monitor on board the Advanced Telescope for High Energy Astrophysics has been proposed and it is currently under study. It will be able to track different species with the necessary accuracy and precision to guarantee the challenging requirement of 2% reproducibility of the background.

Unified Astronomy Thesaurus concepts: Particle astrophysics (96); X-ray detectors (1815); Diffuse x-ray background (384); X-ray astronomy (1810)

1. Introduction

The instrumental background has always played an important role in X-ray missions, limiting the exploitation of scientific data from diffuse sources of low surface brightness such as the intra-cluster medium of galaxy clusters (Molendi 2017). This is painfully true for the data collected by the European Photon Imaging Camera (EPIC) instruments, the two MOS CCD cameras (Turner et al. 2001), and the pn CCD camera (Strüder et al. 2001) on board the ESA XMM-Newton mission (Jansen et al. 2001).

The EPIC instrumental background can be separated into particle and electronic noise components. The knowledge of these components has been growing throughout the entire XMM-Newton lifetime thanks to the many efforts involved in collecting suitable blank sky fields to be used as template background by the XMM-Newton users (Read & Ponman 2003; Carter & Read 2007), the analysis of the XMM-Newton Guest Observer Facility leading to the XMM-Newton Extended Source Analysis Software (Kuntz & Snowden 2008; Snowden et al. 2008), the efforts of the XMM-Newton SOC[6], and the contributions of various research teams, including our own (De Luca & Molendi 2004; Gastaldello et al. 2007; Leccardi & Molendi 2008). A summary table of the EPIC instrumental background components is available at this link[7] based upon Read & Ponman (2003).

The properties (temporal behavior, spectral and spatial distribution) of the signal generated by the interaction of particles with the detectors and with the surrounding structure depend on the energy of the primary particles themselves. Low energy particles (mainly protons with energies of a few tens of kilo electron volts) accelerated in Earth's magnetosphere can reach the detectors as they are concentrated by the telescope mirrors. Their interactions with the CCDs generate events that are indistinguishable from valid X-ray photons and cannot be rejected on board. Sudden increases of the count rate are observed due to these particles, dubbed "soft proton flares." The timescale is extremely variable, ranging from hundreds of seconds to several hours, while the peak count rate can be more than three orders of magnitude higher than the quiescent one. The extreme time variability is the fingerprint of this background component, the Soft Proton (SP) component (see Fioretti et al. 2016 and references therein). This component, totally unexpected before the Chandra and XMM-Newton launch, is now a concern for future X-ray missions. The study of this component in the XMM-Newton data and its connection

---

[6] http://xmm2.esac.esa.int/docs/documents/GEN-TN-0014.pdf

[7] www.star.le.ac.uk/~amr30/BG/BGTable.html

with the Earth's magnetosphere is actively pursued (Walsh et al. 2014; Gastaldello et al. 2017; Ghizzardi et al. 2017; Salvetti et al. 2017; Kronberg et al. 2020, 2021).

High energy particles ($E >$ a few tens of mega electron volts) generate a signal that is mostly discarded on board on the basis of an upper energy threshold and of a pattern analysis of the events (Lumb et al. 2002). The unrejected part of this signal represents an important component of the EPIC instrumental background. The timescale of its variability has always been qualitatively estimated to be much longer than the length of a typical XMM-Newton observation and it has been typically dubbed the "quiescent" background component (also called non X-ray background, NXB, in the literature) as opposed to the flaring SP component. There are two ways to measure the quiescent background in the EPIC detectors: (1) through the analysis of portions of the detector not exposed to the sky (outFOV) where neither sky X-ray photons nor soft protons concentrated by the mirrors are collected there. This is the reason why this component is also dubbed the "un-concentrated" background component and we will use this terminology throughout the paper; (2) through the study of the observations with the filter wheel in closed position (FWC): in this configuration, a 1 mm thick aluminum window prevents X-ray photons and soft protons from reaching the detector. The outFOV regions offer the advantage of a measurement of the unfocused background simultaneous with the observation. FWC observations allow to check and eventually correct for spatial variations of the NXB spectrum across the detector. EPIC MOS has been generally preferred for studies of this component because of the relatively small outFOV pn detector area and for the higher percentage of out of time events (6.3% in full frame operation mode or 2.3% in extended full frame operation mode for the pn as opposed to 0.35% for MOS). Moreover, soft protons contamination of the unexposed area of the pn detector due to a different camera geometry with respect to MOS has recently been documented (Marelli et al. 2021).

Several attempts have been made to gain insight into the origin of the un-concentrated background of X-ray detectors. Hall et al. (2008), through detailed simulations, showed the bulk of the EPIC MOS and pn background can be due to secondary electrons produced by the interaction of cosmic ray protons with the structure surrounding the detectors. More recent work on the WFI (von Kienlin et al. 2018) and XIFU (Lotti et al. 2018) detectors to fly on board the next ESA Large Mission Advanced Telescope for High Energy Astrophysics (ATHENA, Nandra et al. 2013) lead to similar results.

In this paper, we present a detailed characterization of the unfocused XMM-Newton background through the analysis of a large amount of outFOV MOS2 data. The motivation for using only the MOS2 data set is to ensure a data set as uniform as possible with time: we excluded the MOS1 camera from our analysis because of the loss of two peripheral CCDs on 2005 March and on 2012 December. Our goal is to identify the origin of the the EPIC MOS un-concentrated background. To reach it we will employ data from experiments sensitive to particles as well as from other X-ray detectors.

We will use the knowledge we gain to discuss possible improvements to the background characterization of detectors on board ATHENA.

The paper is organized as follows: in Section 2 we describe the preparation and analysis of the XMM-Newton outFOV MOS2 data set. In Section 3, we describe the data sets that we will cross-correlate with the XMM-Newton data: in Section 3.1, the data from the EPHIN detector on board the SOHO satellite; in Section 3.2, the data from Chandra; and in Section 3.3, the data from the EPIC Radiation Monitor (ERM) also on board XMM-Newton. The qualitative similarity of the behavior of the four data sets as a function of time is impressive and, in Section 4, we quantitatively cross-correlate the four data sets. In Section 5, we address the origin of the background enhancements at the end of the XMM-Newton orbits. Results are discussed in Section 6 and summarized in Section 7.

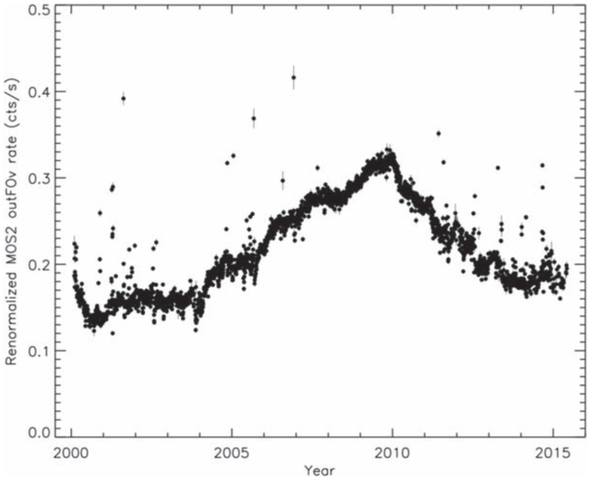

Figure 1. MOS2 outFOV count rate (re-normalized to the area of the full field of view) as a function of time. Each data point is the rate for a single XMM-Newton revolution.

2. The XMM-Newton Data Set

Our data set comprehends all the MOS2 exposures in the observations reported in the 3XMM source catalog distribution 6:[8] 10065 MOS2 exposures over the 9160 public XMM-Newton EPIC observations made between 2000 February 3 and 2015 June 4. Unlike Marelli et al. (2017), we did not make any sub-selection based on the EXTraS project (De Luca et al. 2021), attitude variations, submode, or celestial sources in the in-field-of-view data since they are not relevant for the out-field-of-view (outFOV) analysis.

We applied the same pattern, flags, and energy filters, as well as the same data analysis, reported in Marelli et al. (2017). Light curves of the outFOV were extracted using the methods described in Marelli et al. (2017). We accumulated counts in time bins of 1 ks and we further selected time bins where the minimum number of counts accumulated in the outFOV area was 20 (the latter selection excluded 2.77 Ms of data) to ensure Gaussian errors. This is equivalent to excluding the time bins with a low exposed fraction of their duration as described in Salvetti et al. (2017). The data set explored in this work covers 15 yr of data and it amounts to 255 Ms of data. The plot of all the available data binned in units of the XMM-Newton revolution, which typically lasts 2 days and features an EPIC exposure time of 120 ks, is shown in Figure 1. As we can see, some data points deviate strongly from the general trend followed by the bulk of the data: those are XMM-Newton revolutions affected by Solar Energetic Particle (SEP) events. An example is reported in Figure 2 where we show data from

---

[8] http://xmmssc.irap.omp.eu/Catalogue/3XMM-DR6/3XMM_DR6.html

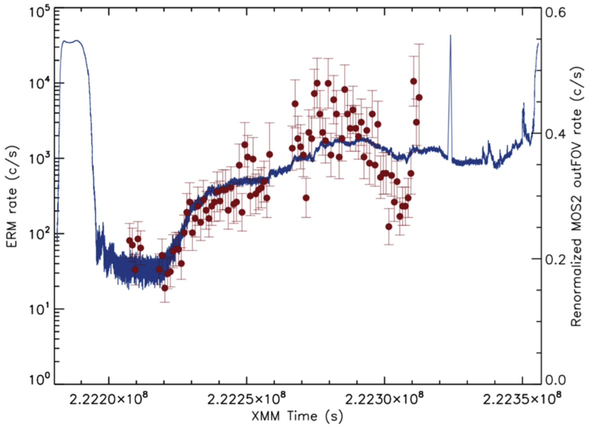

Figure 2. MOS2 outFOV count rate of the data taken during revolution 935 (obsid 0201090201, 0202130301 and 0205340201) binned at 1 ks and plotted as red circles with error bars and the corresponding ERM data in the HES0 channel as the blue solid line.

revolution 935 over-plotted with the corresponding data from the XMM-Newton radiation monitor in the HES0 channel (sensitive to protons in the 8–40 MeV range, see Section 3.3). To filter out XMM-Newton revolutions during SEP events, we used the SEP event list found on the ESA Solar Energetic Particle Environment Modeling (SEPEM) application server.[9] That event list is updated only to 2013 March 15 and, to include more recent SEP events, we adopted the same parameters used for the generation of the reference list, i.e., proton flux above 0.001 $\mathrm{cm}^{-2}\ \mathrm{s}^{-1}\ \mathrm{sr}^{-1}\ \mathrm{MeV}^{-1}$ in the energy channel 7.23–10.46 MeV. We therefore excluded 273 revolutions contaminated by SEP events ($\sim$10% of the 2615 revolutions of our sample). The total amount of time excluded corresponds to 20.2 Ms of data, 8% of our total data and we are left with 235 Ms of data.

We investigated whether some variability is left at the timescale of the length of the typical observing time during a single XMM-Newton revolution. We tested the light curves for each XMM-Newton revolution for variability by calculating a χ^2 test for the null hypothesis of a constant source count rate, flagging as variable light curves with a probability $\leqslant 10^{-5}$ of being constant, as routinely applied in variability studies (e.g., to asses variability in 3XMM sources, Rosen et al. 2016). We found variability in 166 revolutions, 7% of our SEP filtered sample of revolutions; for the great majority of the cases, we found that this variability occurs in last few kiloseconds of the orbit when the XMM-Newton satellite is entering the particle belts. As an example, in Figure 3, we show three light curves of revolutions during different years of the XMM-Newton lifetime as a function of the phase of the XMM-Newton orbit.[10] The origin of these enhancements will be discussed in Section 5.

If we exclude the last periods of data acquisition of the various orbits by excluding data taken at phases of the orbit greater than 0.8, then the number of orbits exhibiting variability decreases to only 14. For these orbits, the variability is in general due to a time bin with a low fractional exposure or, for some early data, when the entrance into the belt happens at smaller phases of the XMM-Newton revolution (e.g., revolution 168 when the entrance into the belts happens at a phase of 0.7). If we exclude these data, we are left with a data set of 2328 revolutions for 208 Ms of data. This will be our final cleaned sample used for the comparison with the external data sets detailed in the following sections and is shown in Figure 4. The overall reduction of scatter in the light curve has been almost totally achieved by the filtering of SEP events; the exclusion of the last phases of the XMM-Newton orbits leads to a correction to the count rate accumulated during each orbit of the order of 1%.

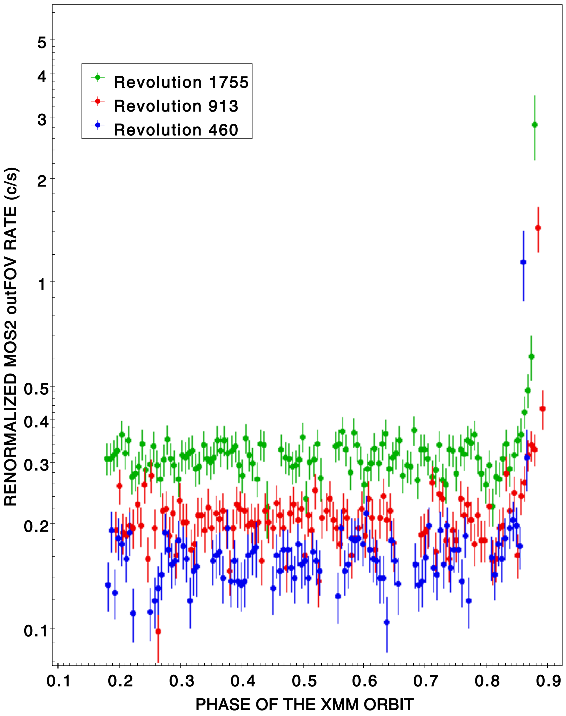

Figure 3. Examples of MOS2 outFOV light curves as a function of the phase of the XMM-Newton orbit showing that the variability is due to a few kiloseconds at the end of the orbit.

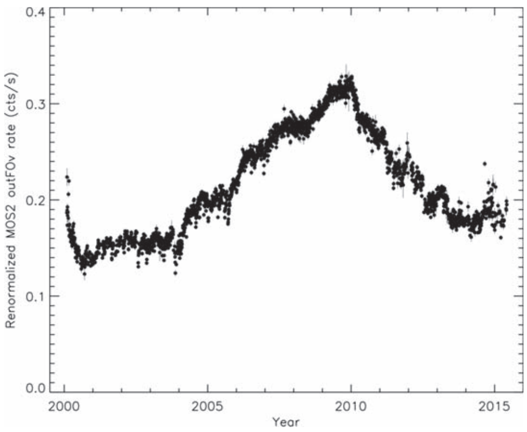

Figure 4. Same as Figure 1 filtered for data taken during SEP events and at the end of the revolution while entering the particle belts.

The only exception to the use of this cleaned data set will be for the discussion in Section 4.3, where we will revert to the use of the data not filtered by SEP events.

---

[9] http://www.sepem.eu/help/event_ref.html

[10] We calculated the phase of the orbit by parsing the TSTART and TSTOP keywords of the orbit file available for each XMM-Newton revolution at the XMM-Newton webpage https://www.cosmos.esa.int/web/xmm-newton/radmon. They are the results of the XMM-Newton Science Analysis Software (SAS) *orbit* task executed with a sample interval of 1 s.

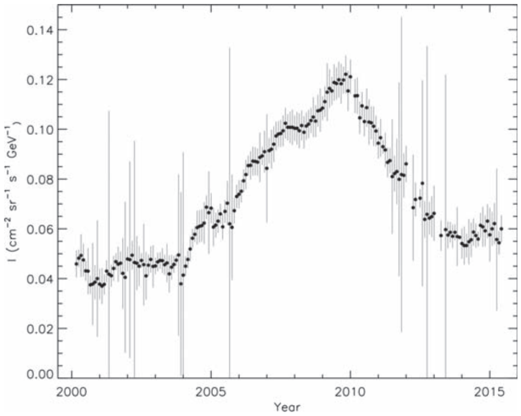

Figure 5. SOHO EPHIN flux in the energy range centered at 1.04 GeV in the time period overlapping the available XMM-Newton data presented in this work.

3. External Data Sets

3.1. SOHO EPHIN Data

To access directly the relevant energy dependent flux of galactic cosmic rays (GCRs) we used measurements from EPHIN on board SOHO. Kühl et al. (2016) have extended the energy range of the instrument to cover the energy range 250 MeV–1.6 GeV, making available a large data set in terms of energy and time coverage (from 1996 to 2015) comparable to the XMM-Newton outFOV data set. Here, we use monthly averaged fluxes measured between 2000 January and 2015 March and we show the data in the energy range centered on 1.04 GeV, see Figure 5. The systematic uncertainties of the fluxes are estimated to be below 20% while, for most of the data points, the statistical uncertainty for GCRs is negligible with respect to the systematic one.

By comparing Figures 4 and 5, we can readily appreciate the similarity between the MOS2 *outFOV* and EPHIN light curves. The quantitative correlation of the data will be discussed in Section 4.1.

3.2. Chandra Rejected High Energy Data

The Chandra X-ray Observatory is in a high-Earth orbit and ACIS, the Advanced CCD Imaging Spectrometer, uses CCDs, much like XMM-Newton. A proxy for the particle background on ACIS is the rate of events that exceed a high energy threshold, ∼15 keV, while the instrument is stowed and not viewing the sky. These events are identified and discarded on board, but the number in each frame is telemetered to the ground. The stowed position ensures that soft protons do not reach the detectors and therefore these data should be similar to MOS2 outFOV data. Figure 6 shows the high energy reject rate for ACIS-S3, a back-illuminated CCD, as a function of time (Grant et al. 2014).[11] Each bin represents a single observation: the mean (and median) exposure time is 8 ks. The shape of the lightcurve of this ACIS background proxy mirrors those of the XMM-Newton MOS2 outFOV rate and of the EPHIN flux. The bulk of the outliers from the general trend can again be identified with SEP events which have been excluded from the analysis adopting the same methodology used for the MOS2 data explained in Section 2.

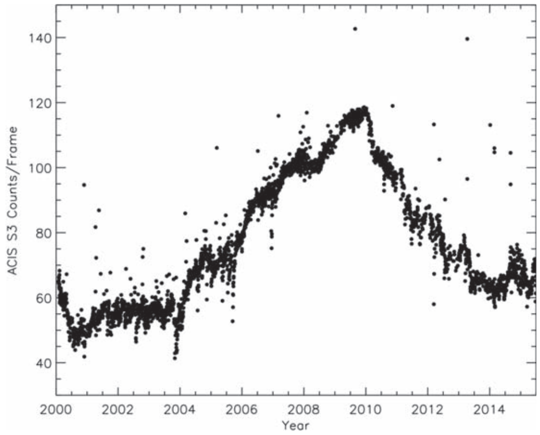

Figure 6. Chandra high energy (>15 keV) count rate for the ACIS-S3 CCD as a function of time. Each data point is the average rate for a single 3–10 ks observation. The *y*-axis range has been clipped to a value of 150 counts frame^{-1} for clarity of the plot.

3.3. EPIC Radiation Monitor

There is an instrument on board XMM-Newton that registers the total count rate and basic spectral information of the background generating radiation: the ERM (Boer et al. 1995). Its main objective is to issue a warning when the intensity of the radiation exceeds a certain level in order to trigger the shutdown of the scientific instruments and protect them from high levels of radiation. The ERM consists of two detectors, the low energy proton and electron unit (LE) and the high energy particle unit (HE). All the units are based on silicon diodes, which record the energy loss in the material. The HE consists of two Si junctions equipped with electronics that register single events (a particle passing through one junction and not the other) and the result is the counting of pulses for a selected energy band, the high energy single (HES) rate. Spectral information is provided by registering the coincidence events for particles which deposit energy in both junctions (high energy coincidence, HEC, rate). The ERM is operated in two different modes, fast and slow: for the slow mode, a complete spectrum is provided every 512 s, whereas, in the fast mode, the spectrum is provided every 4 s. Counting single rates are provided every 4 s in both modes and these rates have been used in this work.

We made use of the HES0 rate, which represents the number of counts accumulated over the all 256 channels of the instrument (as done in a previous study, Gastaldello et al. 2017). The HES0 is sensitive to protons in the 8–40 MeV range and electrons in the 1–1.75 MeV range. For an additional description of the ERM, see this link.[12] The data are available at this link.[13] An example of an ERM light curve is shown in Figure 7 in the various single mode events together with the altitude reached during the orbit by the satellite. This plot highlights the key features exploited in this work. The high ERM rates in the HES0 channel are driven by the passage in the outer electron belt (Métrailler et al. 2019). The outer boundary of the outer electron belt varies in time for two reasons. The first physical reason is that, occasionally, it can grow rapidly when solar eruptions reach the Earth magnetosphere and then deflate (see the review by Baker et al. 2018);

---

[11] http://space.mit.edu/~cgrant/cti/cti120/bkg.pdf

[12] http://www.cosmos.esa.int/web/xmm-newton/radmon-details

[13] https://www.cosmos.esa.int/web/xmm-newton/list-of-tc-radmon

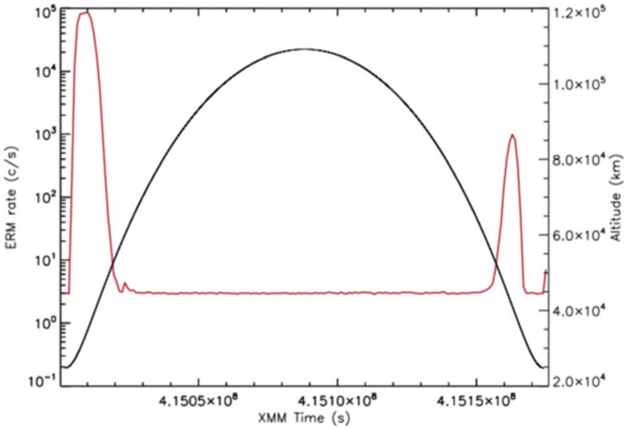

Figure 7. ERM count rates in bins of 1 ks for the HES0 channel (red line). The altitude of the XMM-Newton orbit is over-plotted with a black curve.

the second, and more relevant for our purposes, is that the XMM-Newton orbit goes through phases of higher and lower ellipticities with different altitudes of apogee and perigee (see, e.g., Figure 1 of Walsh et al. 2014). In every revolution, an observing window is defined during which the radiation level is low enough to use the instruments. XMM-Newton turns off the scientific instruments before entering the belts and turns them back on after exiting the radiation belts. The ERM rates for the rest (and great majority of the time) of the orbit reflect the intensities of the Galactic cosmic rays. We therefore used the median of the ERM HES0 count rate in each XMM-Newton orbit (and the median absolute deviation for its error) as a proxy for the background rate encountered by the MOS2 instrument (and, in general, for all the XMM-Newton scientific instruments) during their operations. The plot of this quantity is shown in Figure 8 alongside with the monthly number of Sun spots which is a useful and easy proxy for the solar activity.[14] The plot shows a clear anticorrelation of the ERM rate with the solar activity because the latter modulates GCRs. It also highlights the effectiveness of the median in removing the passage in the belts but not periods of enhanced count rates associated to SEP events.

4. Correlations of the MOS2 outFOV Rate with External Data Sets

The trend with time of the MOS2 outFOV rate (see Figure 4) shows a remarkable similarity with the ones of the EPHIN data (see Figure 5), the Chandra data (see Figure 6) and the ERM data (see Figure 8). To obtain a quantitative comparison, we performed a Bayesian linear regression (Kelly 2007) to estimate a linear relation between the MOS2 outFOV rate and the EPHIN flux (in Section 4.1), between the MOS2 outFOV rate and the Chandra ACIS-S3 rejected high energy rate (in Section 4.2), and between the MOS2 outFOV rate and the ERM rate in the HES0 channel (in Section 4.3). The Bayesian approach has the advantage of treating the intrinsic scatter as a free parameter and it accounts for measurement errors in both the dependent and independent variables. We fitted relations of the form:

$$\hat{Y} = \alpha + \beta\,\hat{X} + \epsilon, \tag{1}$$

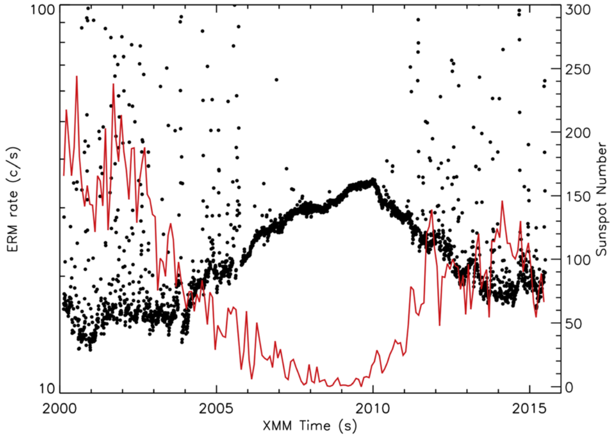

Figure 8. The median count rate of the ERM HES0 in each XMM-Newton orbit is shown as a function of time. The y-axis range has been clipped to a value of 100 counts s^{-1} and error bars have been omitted for clarity of the plot. The number of Sun spots is over-plotted with a red line.

where $X = \hat{X} + \sigma_X$ and $Y = \hat{Y} + \sigma_Y$ with X and Y the measurements and σ_X and σ_Y their respective measurement errors. The free parameters are the intercept, α, the slope, β and the intrinsic scatter about the relation, ϵ. We used the publicly available IDL version, *linmix_err.pro*, of Kelly (2007) code which provides samples from the posterior distribution of the three free parameters. We will quote as best-fit values and their errors for the parameters of the regression fit the mean and standard deviations of the posterior samples provided by the code. For the intrinsic scatter we will quote a percentage scatter, $\epsilon[\%]$, referring to $\epsilon/\,\mathrm{med}(Y)$, the estimated scatter divided by median of the Y values. As the estimate of the intrinsic scatter can be biased in presence of errors which are overestimated, we will also quote the root mean square deviation (RMSD), $\sqrt{\sum_1^n(\hat{Y} - Y)^2/n}$ where n is the number of data points, in percentage terms, $\Delta[\%] = \mathrm{RMSD}/\mathrm{med}(Y)$. This is a measurement of the total scatter thus providing an upper limit to the value of the intrinsic scatter.

To convert from the units seen in the previous plots for the MOS2 outFOV rate (re-normalized to the area of the FOV) of counts s^{-1} to the units used in the next section and plots of counts s^{-1} cm^{-2} keV^{-1}, we used an energy range of 3.7 keV and a geometrical area of 29.078 cm^2 for the MOS2 FOV (Marelli et al. 2017).

4.1. *The Correlation of the MOS2* outFOV *with SOHO EPHIN Data*

The GCR-induced background has been measured through the analysis of the corners of the MOS2 detector (MOS outFOV) not exposed to the sky where neither X-ray photons nor soft protons penetrate. We matched the MOS outFOV data with the monthly averaged EPHIN fluxes by estimating the monthly outFOV count rate obtained by summing all the counts accumulated during that month and dividing it by the corresponding summed exposure time. The correlation with EPHIN fluxes for protons with energies greater than 681 MeV is very good and we show as an example the correlation with the energy of 1.04 GeV (see Figure 9). The relation features a very low intrinsic scatter of about 0.8% ± 0.4%. Being aware of the possible underestimate of this quantity by the

---

[14] Data taken from http://sidc.oma.be/silso/datafiles.

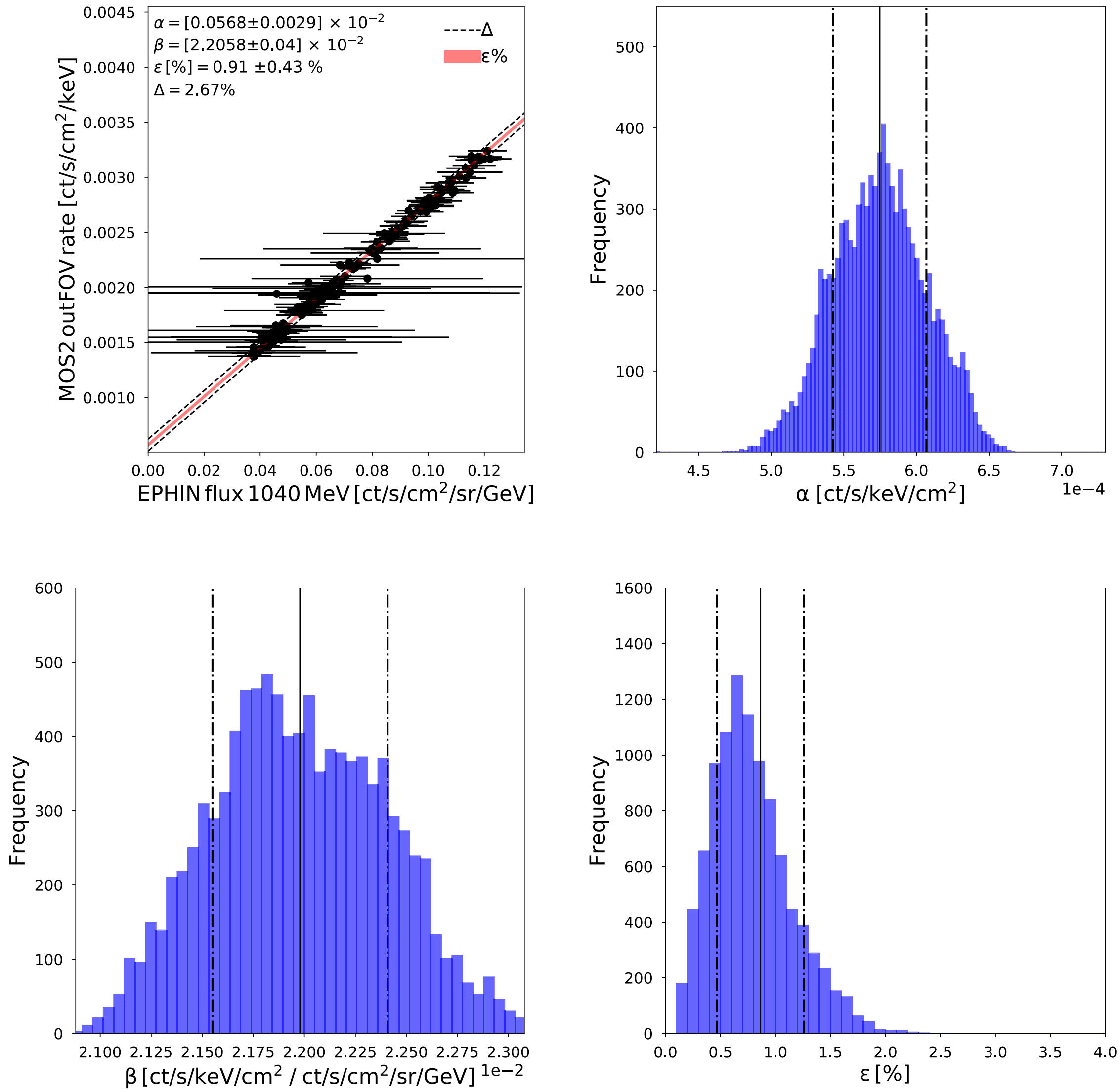

Figure 9. Correlation of the XMM-Newton MOS2 outFOV rate with the SOHO EPHIN proton flux at 1040 MeV. In the top left panel, the data and the best-fit relation are shown, together with the shaded area highlighting the intrinsic and total scatter. In the other panel, the samples of the posterior distribution of the three fitted parameters as provided by the *linmix* code are shown: the intercept α (top right panel), the slope β (bottom left panel), and the percentage intrinsic scatter $\epsilon[\%]$ (bottom right panel).

conservative estimate of the EPHIN systematic error, we also report the total scatter which is 2.6%, still very low.

4.2. *The Correlation of the MOS2* outFOV *Rate with Chandra ACIS-S3 Reject Rate*

The same qualitative time behavior is also seen in the Chandra ACIS-S3 reject rate, a proxy for the unfocused background component in Chandra (see Figure 6). We cross-correlated the two data sets by matching the time of the stowed Chandra observation with the corresponding XMM-Newton revolution which is the time bin used in Figure 10. Notwithstanding some outliers still present even after the removal of SEP events, the correlation is very good also in this case: the linear relationship connecting the two rates has an intrinsic scatter of 5.3% ± 0.1% and a total scatter of 7% (see Figure 10).

4.3. *The Correlation of the MOS2* outFOV *Rate with ERM*

The plot shown in Figure 7 highlights the fact that taking the median of the count rates in the ERM HES0 channel during the orbit is effective in removing features due to passage in the belts. This is not the case for periods of enhanced count rates lasting for more than an XMM-Newton orbit and associated with SEP events, see Figure 2 for an example. Belt passages and SEPs are periods where the count rates in the HES0 channel do not reflect the GCR particle population. This is highlighted by the plot in Figure 11 (left panel) where we simply compare the orbit-averaged MOS2 outFOV rate shown in Figure 1 with the median of the HES0 count rate in the same orbit. The HES0 ERM count rate varies by more than two orders of magnitude however the unfocused background varies at most by a factor of two. If we exclude the XMM-Newton orbits flagged as affected by SEP events as discussed in Section 2, we obtain a cleaner correlation as shown in the right

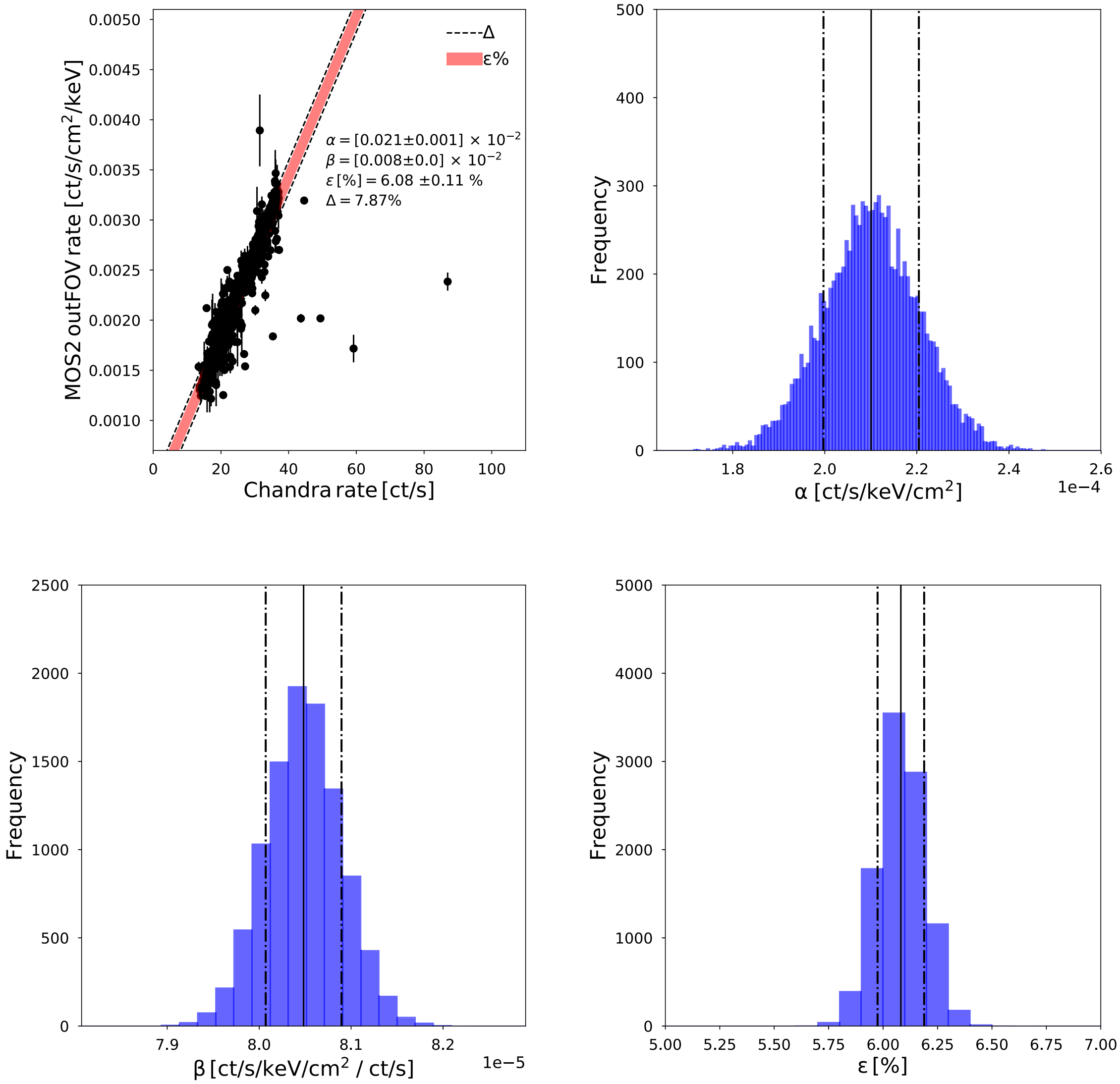

Figure 10. Correlation of the MOS2 outFOV rate with the Chandra ACIS-S3 reject rate. The outline of the figure is the same as the one of Figure 9 with the data, the best-fit relation and the total and intrinsic scatter shown in the top left panel and the posterior for the three fitted parameters of the relation in the other panels: the intercept α (top right panel), the slope β (bottom left panel), and the percentage intrinsic scatter $\epsilon[\%]$ (bottom right panel).

panel of Figure 11. The remaining outliers are quite likely associated to SEP events as the time duration of a SEP event can be underestimated in some cases by satellites on low Earth orbit (see the example shown by Gastaldello et al. 2017). The same explanation can be put forward for the outliers in the correlation between the MOS2 outFOV rate and the Chandra ACIS-S3 reject rate (see Section 4.2).

With this filtering, the scatter in this correlation becomes low as quantified by the linear fit shown in Figure 12: the intrinsic scatter is at the level of $2.3\% \pm 0.1\%$ and the total scatter is the level of 4.5%.

5. Enhancements in the Last Phases of the XMM-Newton Orbit

Having established that enhancements observed in the MOS2 outFOV can, in most instances, be attributed to SEP events, we are left with the question of the origin of those occurring at the end of XMM-Newton orbits. To address this point, we have performed a case study of the closed observation taken during the routine calibration observation in revolution 1413 (obsid 0510780101). Closed observations at the end of the orbit can last more than the science exposures and data can be extracted by the entire field of view as they are not contaminated by soft protons. The light curve (see the left panel of Figure 13) shows the enhancement and has been divided in three time intervals: a low-intensity behavior range seen throughout the typical science observations, a medium intensity range, and a high intensity range. Spectra taken at these different levels of intensity are shown in the right panel of Figure 13 with the same color coding. The canonical empirical model used to fit the GCR-induced background usually present in the XMM-Newton data (broken power-law model plus Gaussians for the fluorescence lines) is applied to the spectra extracted during the three time intervals. A statistically significant change in the high energy slope of the continuum is evident, going from the typical value of the unfocused MOS background of 0.18 ± 0.01 to 0.35 ± 0.01 in the high state. Residuals associated with the best-fit model of the low-intensity data are also shown, highlighting the change of slope of the continuum.

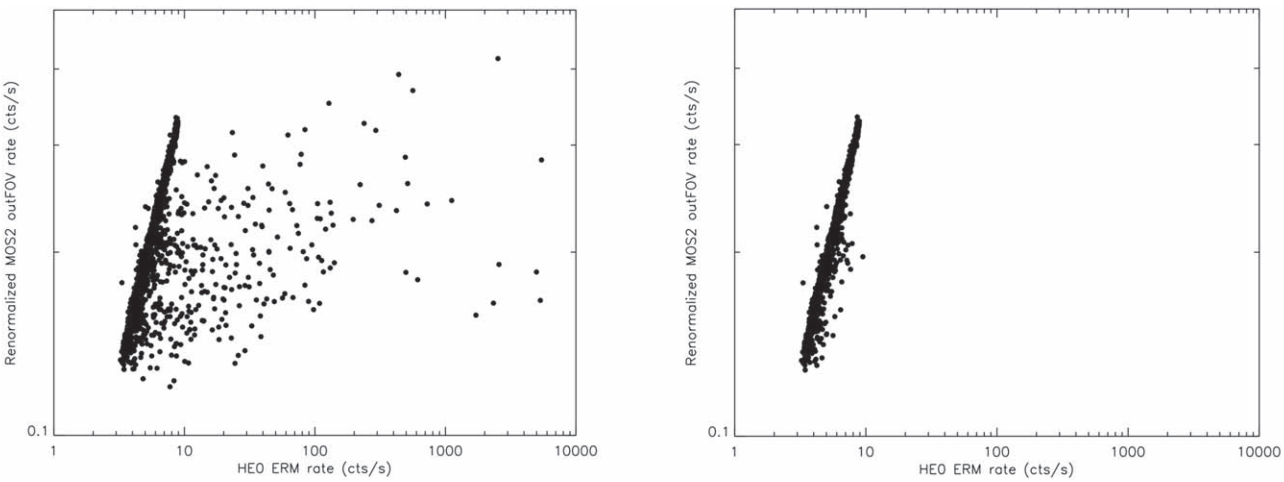

Figure 11. Left panel: comparison of the average MOS2 outFOV rate with the median ERM HES0 rate in the same XMM-Newton orbit. Right panel: same as the left panel but omitting revolutions flagged as affected by SEP events.

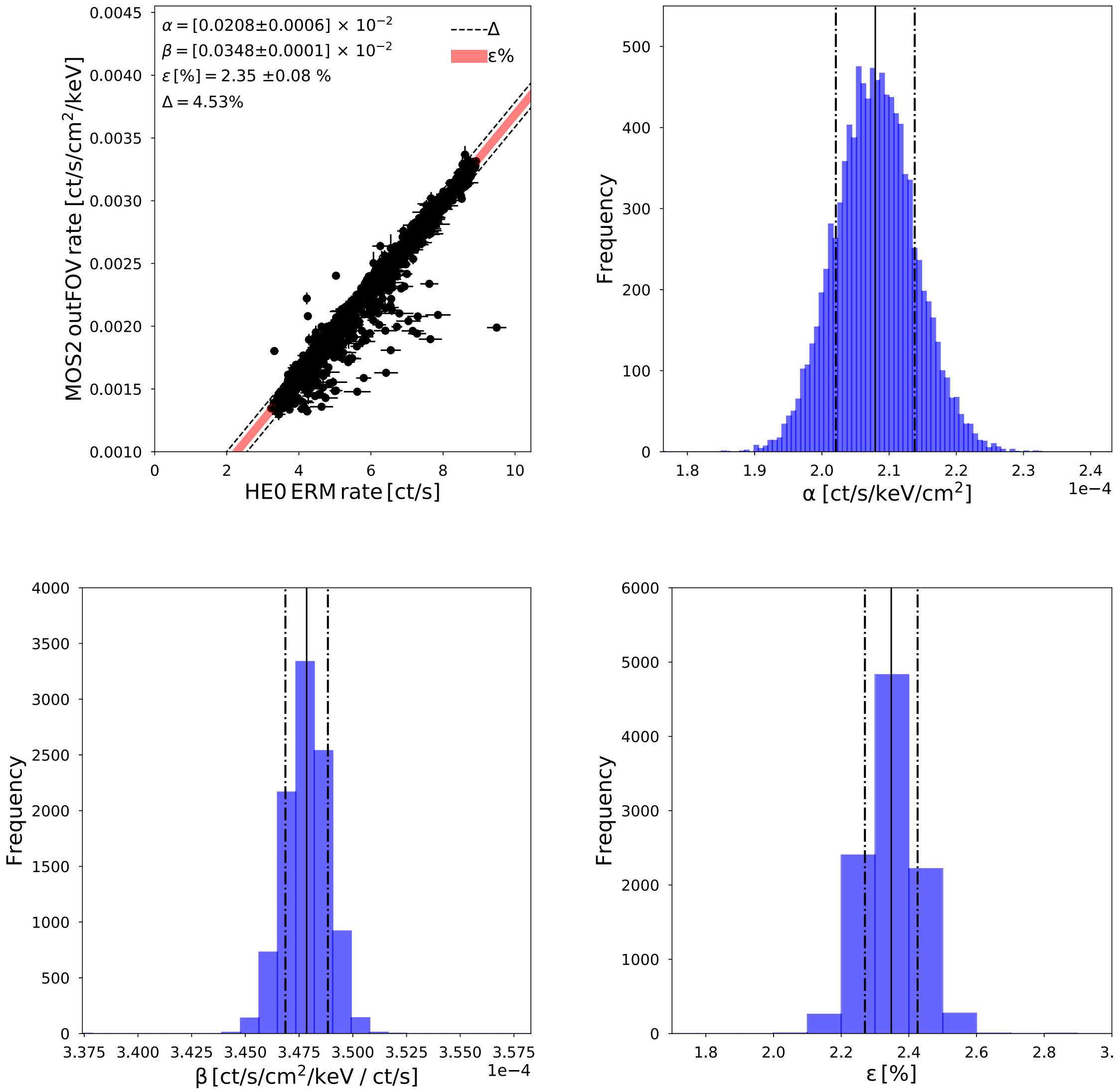

Figure 12. Correlation of the MOS2 outFOV rate with the ERM HES0 rate. The panels show the quantities in a similar way as for Figures 9 and 10.

A similar result is obtained by stacking the outFOV data from the last few (of the order of 5–10) kiloseconds of data at the end of the each orbit. If we accumulate spectra for time bins where the count rate exceeds the median count rate of the revolution by a factor of 1.6 at least (as a convenient operational way to identify the excess at the end of the orbits),

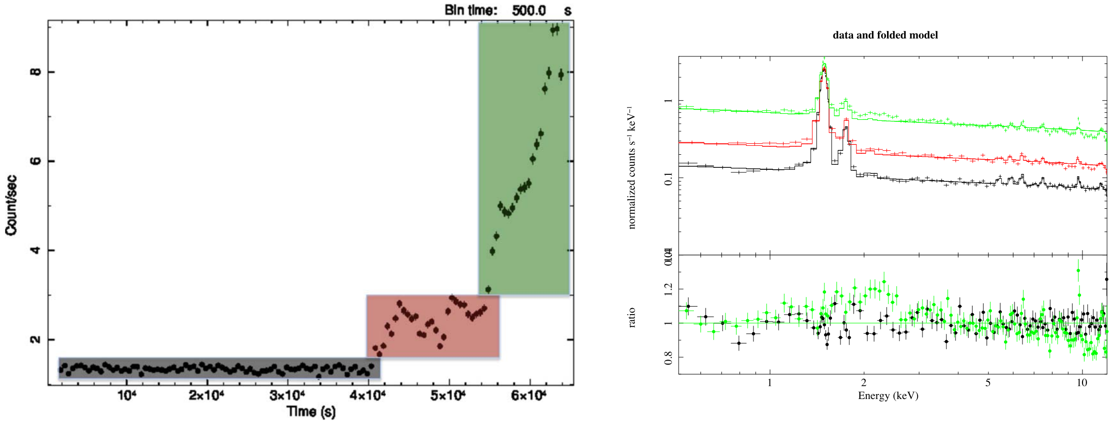

Figure 13. Left panel: the count rate of the entire MOS2 detector in the energy band 0.5–12 keV as a function of time during the closed observation with obsid 0510780101 S005. The three time intervals are highlighted for which spectra have been extracted (see right panel) Right panel: spectra extracted from the different time intervals shown in the left panel with the same color coding: low count rate (black), intermediate count rate (red), and high count rate (green). The best-fit broken power-law plus Gaussian fluorescent lines of the low-count-rate spectrum is applied to the three spectra to highlight the change in the slope in the continuum, as also shown by the residuals of the model of the low and high count-rate spectra.

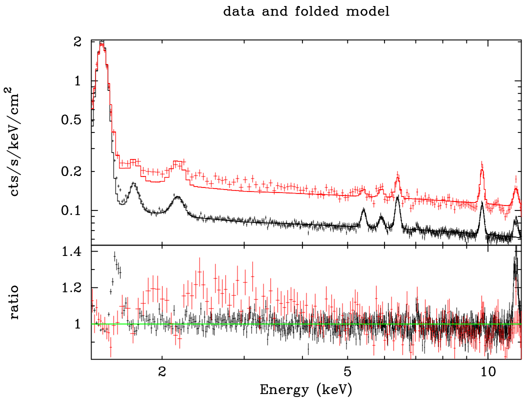

Figure 14. MOS spectra accumulated from the entire revolution, in black, and from phase >0.5 and times bins with rate larger than 1.6 times the median revolution rate, in red. The canonical background model is fit to the first spectrum and then applied to the second. In the bottom panel, where we show residuals in the form of a ratio of data to model, we can observe how the spectrum collected during intensity enhancements at the end of the revolution is steeper than the typical background spectrum.

we obtain the spectrum shown in red in Figure 14, which bears strong similarities with the one plotted in green in Figure 13: the high energy slope is 0.39 ± 0.02 in good agreement with the measurement performed in the high state of the case study of the closed observation. A discussion on the implications of these results will be provided in Section 6.2.

6. Discussion

Analysis of the temporal variability of the MOS2 outFOV data and of ancillary data sets has allowed us to uncover significant correlations. In this section, we will discuss the implications of our findings.

6.1. Correlation with GCR Protons

The tight correlation between the un-concentrated MOS2 background rate and the EPHIN proton flux, see Figure 9, strongly suggests the latter is responsible for the former. This is consistent with findings from detailed Geant4 simulations of the interaction between high energy protons and the ATHENA WFI experiment (von Kienlin et al. 2018), which show the bulk of unrejected background is indeed produced by CR protons. Moreover, the strong correlation observed between EPIC MOS2 and Chandra ACIS-S3 background rates, see Figure 10, can be understood in terms of the common dependency of both on high energy proton fluxes.

Since SOHO EPHIN is in orbit around L1 and XMM-Newton and Chandra are on high-Earth orbits, the variation in cosmic ray protons fluxes between these two locations must be very modest. This is confirmed by the good correlation found when comparing proton fluxes from EPHIN SOHO with those recorded from the radiation monitor on board Chandra (essentially a copy of the EPHIN; see Kühl et al. 2016). These results are in agreement with our current understanding of how cosmic rays vary within the heliosphere, (e.g., Potgieter & Vos 2017). These findings complement and extend those presented in a recent paper (Marelli et al. 2021) where we showed a correlation between SOHO EPHIN proton fluxes and EPIC pn background rates. Modulation with the solar cycle has also been found in the pn closed data taken in small window mode (Bulbul et al. 2020).

This fact is further strengthened by the similar tight correlation found between the XMM-Newton MOS 2 background and the Chandra background (see Section 4.2), which points to the common origin for the background related to GCR protons for CCDs, which are in similar orbits.

Having established that the MOS2 background is mostly driven by high energy protons, we turn to the looser correlation found between ERM rates and the MOS2 background rate (see Figure 11 left panel). The ERM sensitivity peaks around a few mega electron volts, at these energies protons of solar origin provide a significant and highly variable contribution. Removal of the most obvious SEP can improve the correlation (see Figure 11 right panel) at the cost of losing the ability to monitor the particles during SEP events. Moreover, such a strategy would likely require the use of an external experiment to signal time intervals affected by SEPs. These considerations show how traditional radiation monitors, such as the ERM and the ESA Standard Radiation Environment Monitor (SREM, e.g., Evans et al. 2008) are of limited value when trying to characterize the high energy particle component responsible for the instrumental background of X-ray detectors. This can also be understood because the goal of onboard radiation monitors is the protection of the scientific payload instruments in case of excessive radiation. Clearly, instrumentation sensitive to higher energy protons, such as the SOHO EPHIN, is far more suitable. These findings have lead us to propose an ATHENA High Energy Particle Monitor (AHEPaM) operating at the high energies populated by the particles responsible for the un-concentrated ATHENA WFI and XIFU background.

6.2. Electron Contribution

In Section 5, we have shown that, at the end of revolution 1413, the background rate registered in the MOS2 corners suffered a substantial increase (Figure 13, left panel) accompanied by a change in spectral shape (Figure 13, right panel). Since the increase occurred at a time when XMM-Newton was entering the outer electron belts (Métrailler et al. 2019), we attribute the spectral variation to a change in dominant contribution to background generating particles from cosmic ray protons to outer belt electrons. Beyond this single case evidence, a systematic analysis of the MOS2 corner data (see Figure 14) has shown the change in spectral shape to be typical of the last part of the orbit, when XMM-Newton descends into the outer belts. While practical use of this finding for EPIC may be limited, it provides an important cross validation of Geant4 simulations showing that electrons contribute to the total WFI unrejected background (von Kienlin et al. 2018). Moreover, since electrons are likely the only species for which a solar contribution to the ATHENA background might be significant, at least during very energetic SEPs, AHEPaM will be designed to be sensitive to electrons with energies down to 50 MeV.

6.3. Compton Scattering of Cosmic X-Ray Background Hard X-Ray Photons

The MOS2 versus EPHIN correlation (see Figure 9) shows evidence for a "constant" component whose intensity is given by α, the constant term in the linear relation of Equation (1). We interpret this as evidence for a contribution to the un-concentrated particle background that is distinct from the CR component. Similar evidence has been found when correlating the pn un-concentrated background with the EPHIN flux and is discussed in Marelli et al. (2021). As in that paper, we estimate an upper and lower bound to the constant component by repeating the correlation analysis between MOS2 and EPHIN data using different proton channels for the EPHIN data: taking as representative the values of the correlations at 500 MeV and 1.2 GeV, we find that, in the former case, the constant term is $\sim 1.1 \times 10^{-3}$ counts s^{-1} cm^{-2} keV^{-1} and, in the latter case, the constant term is $\sim 5 \times 10^{-4}$ cts s^{-1} cm^{-2} keV^{-1}. Those values are a factor of $\sim$2.5 lower than the ones found for the pn.

In Marelli et al. (2021), we presented a thorough discussion of possible origins of this component, the arguments presented there apply here. Briefly, we can exclude the constant as an artifact in our data analysis because the MOS2 and EPHIN data sets have been collected and analyzed independently and cross-correlated only at the end. We can also exclude the constant component associated with cosmic rays or to activation, as it does not vary with the solar cycle. The most likely interpretation is that the constant component is produced by cosmic X-ray photons with energies around 100 keV that Compton scatter electrons within the MOS2 detector. The up-scattered electrons provide a signal that is indistinguishable from that of an X-ray photon and, if their energy falls within the science band, contribute to the MOS2 background. The contribution is constant in time and does not vary when reorienting the satellite because it results from the integrated hard X-ray emission from the whole sky.

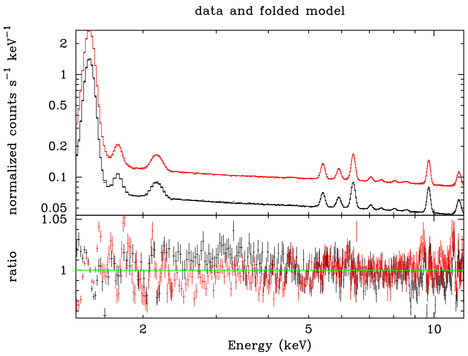

Figure 15. MOS2 Spectra accumulated from the outFOV data at solar maximum (black) and solar minimum (red). In the top panel, we show a fit with a broken power-law model and Gaussian lines with all the parameters linked with the exceptions of the normalizations. Computation of the equivalent width for the lines shows consistent values; for the stronger ones, differences are below a few percent. In the bottom panel, we show residuals in the form of a ratio of data over model showing overall good agreement (see discussion in the text).

We indirectly assessed the spectral shape of the Compton component by accumulating the background from the outFOV data at the solar maximum and at the solar minimum (see Figure 15). We fitted again the canonical GCR-induced background model of a broken power-law model plus Gaussian lines with all the parameters linked between the two spectra with the exception of the normalization. The agreement is good down to a few percent, with the only significant difference found between 2 and 4.5 keV where the solar maximum spectrum shows a $\sim$3% excess with respect to the solar minimum spectrum. This can be related either to a bona fide signature of the Compton component (emerging at solar maximum, when the contribution from GCR is minimum) or, just as likely, to some unknown systematic in the analysis. However it is relatively safe to conclude that the lack of significant changes at times when the contribution of the Compton component to the total background varies substantially suggests that it must be similar in spectral shape to the GCR-induced one.

Comparison of the pn versus EPHIN plot presented in Marelli et al. (2021) with MOS2 versus EPHIN presented here shows a difference in the constant term. This can be accommodated, at least qualitatively, within the framework of the Compton model, by postulating that it relates to the difference in thickness of the active region in the two detectors, about 45 μm for MOS2 and 280 μm for pn. The ratio between the two thicknesses is about 6 which is consistent, within a factor of 2, with the ratio between the pn and MOS constant components. We speculate that the higher sensitivity of the MOS2 detector to the Compton component could be due to a substantial field-free region missing in the fully depleted pn. Electrons suffering a Compton scattering in this region generate a charge cloud that could end up being at least partially collected by the CCD. Since Compton photons have energies of the order of 100 keV, even a partial charge collection could lead to an event in the science band.

An additional contribution in the MOS detector with respect to the pn comes from the time spent during readout of the signal in the storage area. The readout time equals the frame time (2.6 s) and the storage area is 3/10 of the CCD area. The storage area is shielded by a 3.2 mm thick layer of an Al alloy (T. Abbey & D. Ross 2022, private communication) which is however basically transparent to hard X-ray photons producing the Compton signal. As a benchmark, the mean free path for Compton scattering of a 100 keV photon in Al is 2.7 cm.

A more thorough investigation of the issue of the Compton-induced background would require a detailed simulation of the interaction between hard X-ray photons and the EPIC pn and MOS cameras, which is beyond the scope of this paper.

7. Summary

The main findings presented in this paper may be summarized as follows.

1. The tight correlation found between MOS2 background and EPHIN proton flux strongly suggests the bulk of the MOS2 un-concentrated background is generated by GCR protons.
2. The tight correlation between the MOS2 background and the Chandra background reinforces the common origin related to GCRs for CCDs which are in similar orbits.
3. The weaker correlation found between MOS2 background and ERM data results from the significant solar contribution to protons at the MeV energies where ERM sensitivity peaks. Only with appropriate filtering of solar particles the correlation can be tightened.
4. These results show how traditional radiation monitors, such as the ERM and the ESA SREM are of limited value when trying to characterize the high energy particle component responsible for the instrumental background of X-ray detectors. Instrumentation sensitive to higher energy protons, such as the SOHO EPHIN, is far more suitable.
5. A single case study, later corroborated by a systematic analysis of the MOS2 corner data, has highlighted spectral change in EPIC MOS2 background when XMM-Newton descends into the outer belts. We interpret this as evidence of a substantial increase in the electron contribution to the EPIC MOS2 background.
6. As for the EPIC pn, for EPIC MOS we find evidence of a constant component independent of CR particles. Following (Marelli et al. 2021) we attribute this component to Compton scattering of hard Cosmic X-ray photons in the MOS2 detector. The smaller intensity found in MOS2 with respect to pn is in qualitative agreement with the smaller thickness of the former detector with respect to the latter.

Findings presented in this paper and in Marelli et al. (2021) have lead to the formulation of a conceptually new particle monitor for the ATHENA mission: the AHEPaM that is currently under study.

We acknowledge support from the Horizon 2020 Programme under the AHEAD2020 project (grant agreement No. 871158). F.G., S.M., A.D.L., and A.T. acknowledge support from the INAF mainstream project "Characterizing the background of present and future X-ray missions" 1.05.01.86.13. This research has made use of data produced by the EXTraS project, funded by the European Union's Seventh Framework Programme under grant agreement No. 607452. The scientific results reported in this paper are based on observations obtained with XMM-Newton, an ESA science mission with instruments and contributions directly funded by ESA Member States and NASA. The SOHO/EPHIN project is supported under Grant 50 OC 1702 by the German Bundesministerium für Wirtschaft through the Deutsches Zentrum für Luft- und Raumfahrt (DLR). We would like to thank Kip Kuntz and Perry Brendan for useful discussion and advice about the treatment of the pseudo-logaritmic data compression in the ERM data. We would like to thank Tony Abbey and Duncan Ross for providing the drawings and the specifications of the MOS frame storage shield and for helpful discussions. We would like to thank Nicola La Palombara for helpful discussions and insights.

ORCID iDs

Fabio Gastaldello https://orcid.org/0000-0002-9112-0184
Martino Marelli https://orcid.org/0000-0002-8017-0338
Iacopo Bartalucci https://orcid.org/0000-0001-7703-9040
Andrea Tiengo https://orcid.org/0000-0002-6038-1090

References

Baker, D. N., Erickson, P. J., Fennell, J. F., et al. 2018, SSRv, 214, 17
Boer, M., Naya, J., Chabaud, J. P., et al. 1995, ITNS, 42, 2010
Bulbul, E., Kraft, R., Nulsen, P., et al. 2020, ApJ, 891, 13
Carter, J. A., & Read, A. M. 2007, A&A, 464, 1155
De Luca, A., & Molendi, S. 2004, A&A, 419, 837
De Luca, A., Salvaterra, R., Belfiore, A., et al. 2021, A&A, 650, A167
Evans, H. D. R., Bühler, P., Hajdas, W., et al. 2008, AdSpR, 42, 1527
Fioretti, V., Bulgarelli, A., Malaguti, G., Spiga, D., & Tiengo, A. 2016, Proc. SPIE, 9905, 99056W
Gastaldello, F., Buote, D. A., Humphrey, P. J., et al. 2007, ApJ, 669, 158
Gastaldello, F., Ghizzardi, S., Marelli, M., et al. 2017, ExA, 44, 321
Ghizzardi, S., Marelli, M., Salvetti, D., et al. 2017, ExA, 44, 273
Grant, C. E., Bautz, M. W., Ford, P. G., & Plucinsky, P. P. 2014, Proc. SPIE, 9144, 91443Q
Hall, D., Holland, A., & Turner, M. 2008, Proc. SPIE, 7021, 70211Y
Jansen, F., Lumb, D., Altieri, B., et al. 2001, A&A, 365, L1
Kelly, B. C. 2007, ApJ, 665, 1489
Kronberg, E. A., Gastaldello, F., Haaland, S., et al. 2020, ApJ, 903, 89
Kronberg, E. A., Hannan, T., Huthmacher, J., et al. 2021, ApJ, 921, 76
Kühl, P., Gómez-Herrero, R., & Heber, B. 2016, SoPh, 291, 965
Kuntz, K. D., & Snowden, S. L. 2008, A&A, 478, 575
Leccardi, A., & Molendi, S. 2008, A&A, 486, 359
Lotti, S., Macculi, C., D'Andrea, M., et al. 2018, Proc. SPIE, 10699, 106991Q
Lumb, D. H., Warwick, R. S., Page, M., & De Luca, A. 2002, A&A, 389, 93
Marelli, M., Molendi, S., Rossetti, M., et al. 2021, ApJ, 908, 37
Marelli, M., Salvetti, D., Gastaldello, F., et al. 2017, ExA, 44, 297
Métrailler, L., Bélanger, G., Kretschmar, P., et al. 2019, AdSpR, 64, 1701
Molendi, S. 2017, ExA, 44, 263
Nandra, K., Barret, D., Barcons, X., et al. 2013, arXiv:1306.2307
Potgieter, M. S., & Vos, E. E. 2017, A&A, 601, A23
Read, A. M., & Ponman, T. J. 2003, A&A, 409, 395
Rosen, S. R., Webb, N. A., Watson, M. G., et al. 2016, A&A, 590, A1
Salvetti, D., Marelli, M., Gastaldello, F., et al. 2017, ExA, 44, 309
Snowden, S. L., Mushotzky, R. F., Kuntz, K. D., & Davis, D. S. 2008, A&A, 478, 615
Strüder, L., Briel, U., Dennerl, K., et al. 2001, A&A, 365, L18
Turner, M. J. L., Abbey, A., Arnaud, M., et al. 2001, A&A, 365, L27
von Kienlin, A., Eraerds, T., Bulbul, E., et al. 2018, Proc. SPIE, 10699, 106991I
Walsh, B. M., Kuntz, K. D., Collier, M. R., et al. 2014, SpWea, 12, 387